Diffusely scattered and transmitted elastic waves by random rough solid-solid interfaces using an elastodynamic Kirchhoff approximation

Fan Shi* and Mike Lowe
Department of Mechanical Engineering, Imperial College London, London, United Kingdom

Richard Craster
Department of Mathematics, Imperial College London, London, United Kingdom

(Received 16 January 2017; revised manuscript received 23 May 2017; published 13 June 2017)

Elastic waves scattered by random rough interfaces separating two distinct media play an important role in modeling phonon scattering and impact upon thermal transport models, and are also integral to ultrasonic inspection. We introduce theoretical formulas for the diffuse field of elastic waves scattered by, and transmitted across, random rough solid-solid interfaces using the elastodynamic Kirchhoff approximation. The new formulas are validated by comparison with numerical Monte Carlo simulations, for a wide range of roughness (rms $\sigma \leqslant \lambda/3$, correlation length $\lambda_0 \geqslant$ wavelength λ), demonstrating a significant improvement over the widely used small-perturbation approach, which is valid only for surfaces with small rms values. Physical analysis using the theoretical formulas derived here demonstrates that increasing the rms value leads to a considerable change of the scattering patterns for each mode. The roughness has different effects on the reflection and the transmission, with a strong dependence on the material properties. In the special case of a perfect match of the wave speed of the two solid media, the transmission is the same as the case for a flat interface. We pay particular attention to scattering in the specular direction, often used as an observable quantity, in terms of the roughness parameters, showing a peak at an intermediate value of rms; this rms value coincides with that predicted by the Rayleigh parameter.

DOI: 10.1103/PhysRevB.95.214305

I. INTRODUCTION

Interface and surface roughness is well known to significantly alter the elastic wave scattering field in solids [1], and hence has considerable effects on ultrasonic applications [2–5], and on boundary phonon scattering to model thermal transport in nanostructures [6–11]; on the atomic scale, the phonon-interface interaction can still be modeled by the macroscopic theory on elastic wave scattering in the long-wavelength limit [12]. These important applications have therefore motivated considerable work on rough surface scattering, however, many studies are simply for acoustics [6,9,12,13], that is, for solids omitting shear, and this is a substantial simplification as elastic solids support both bulk shear and compressional waves. Moreover, these bulk waves have different wave speeds and undergo mode conversion upon reflection/transmission at an interface. An elastic stress-free surface also supports Rayleigh surface waves, and an interface supports Stoneley interfacial waves, and acoustic models fail to capture these: here we make no such simplification. There are other natural limits based upon the ratio of the dominant length scales in the problem, here the correlation length, the wavelength, and the root-mean-squared (rms) height, and we shall concentrate here upon the situation where the correlation length is larger than the wavelength and then physically we can use the Kirchhoff approximation, but we shall not invoke any assumption of small rms values. As Maznev [10] notes, there is a heavy reliance upon numerical simulation, a lack of analytical results to draw upon, and open problems remain regarding scattering as a function of correlation length and/or roughness height.

Typical previous approaches study the scattering from a stress-free rough surface, rather than an interface separating two media, in which case the expected scattering is modeled from the knowledge of the statistics of the surface profile. The expected scattering in the specular direction, defined as the specularity, is a widely used parameter to model the phonon transport through a rough interface, and this specularity significantly affects the efficiency of terahertz phonon devices [8,10–12]. Many of the previous studies rely on using the coherent scattering intensity I^c at the specular direction [9,13–17] as proposed, for instance, by Ogilvy [1]:

$$I^c = I^{\text{flat}} \exp(-g_{\alpha\beta}), \quad \alpha,\beta = p,s$$
$$g_{\alpha\beta} = (k_\alpha \cos\theta_i + k_\beta \cos\theta_s)^2 \sigma^2, \tag{1}$$

where I^{flat} is the scattering intensity from a flat surface, and ignore the diffuse scattered field. In Eq. (1), $k_{\alpha/\beta}$ represents the wave number for incident/scattered waves, which can be either a compressional (P) or shear (S) mode. The wave number $k_{\alpha/\beta}$ equals to $\frac{\omega}{c_{\alpha/\beta}}$, where $c_{\alpha/\beta}$ refers to the wave speed and ω is the angular frequency. The incidence and scattering angles are denoted as θ_i and θ_s, and σ is the rms value of the surface height. Many studies regarding phonon boundary scattering have applied a simpler similar equation ascribed to Ziman [18], although it does not include the elastic mode conversion and oblique incidence/scattering angles as Eq. (1) does. Equation (1) considers only the reflection case for a stress-free boundary condition (i.e., solid-air interface); the transmission case needs a different formula, which we derive in this article.

It is well established that Eq. (1) is only valid in the specular direction for surfaces with a very small roughness

*f.shi12@imperial.ac.uk

(e.g., $k\sigma \ll 1$ and $k\lambda_0 \gg 1$). Additional contributions to the total scattering field from the diffuse waves, which sometimes are comparable with, or even dominant over, the coherent field, are not included in the formula. The importance of the diffuse field has been highlighted by a number of reports [10,12,19]. Experiments [9,20] on the thermal transport in nanostructures have indicated that the use of Eq. (1) is often inconclusive and does not explain the experimental findings, requiring alternative theories to account for the diffuse field. In addition Maznev [10] has shown that using Eq. (1) to calculate the specularity tends to overestimate the heat flux dissipation due to loss of the diffuse field.

To model the diffuse scattering from rough boundaries, it has been necessary to utilize sophisticated numerical techniques that have been developed recently, based around the finite-element (FE) method [4,21], the Green's function method [22], and molecular dynamic model [23]. These numerical methods require considerable computation resources and it is not easy to generalize conclusions of how the surface statistics affect the scattering beyond the specific cases simulated unless the statistics are gathered from many multiples of such simulations. Hence there is substantial motivation to develop analytical tools to tackle these problems.

Analytical methods have the advantage that they offer physical insight into the scattering behavior, provided the method is within their region of validity. A perturbation approach, assuming the roughness amplitude is small relative to wavelength, and surface slopes are also small, has been applied recently [8,10], to study the effect of roughness and material properties on the scattering of the diffuse field. However, such a perturbation theory is only valid for modeling scattering from weakly rough surfaces ($\sigma \leqslant \lambda/10$ for the first-order approximation [24]). One important question posed by Maznev [10] concerns the possibility of finding a complementary theoretical method to model the scattering beyond the validity of the perturbation approximation, for surfaces with median and high roughnesses: at high roughness (large rms value) the diffuse field dominates and the scattering is completely different from that with a weakly rough surface.

In this article we develop a theoretical method that is valid for surfaces with a wide range of roughness by using the elastodynamic Kirchhoff approximation (KA). The KA has been found to be accurate in modeling the scattering from surfaces with roughness up to $\sigma = \lambda/3$, when the correlation length λ_0 is comparable with or larger than one wavelength [25,26]. Despite the early application of KA in acoustics [25], it is only recently that the elastodynamic KA has been developed to model theoretically the diffuse field from an elastic rough surface including mode conversions [5]; there are details in elasticity, the mode conversion at surfaces, two types of bulk waves, that prevent a direct generalization. In [5] only a single medium is considered and the rough surface is assumed to be stress free, hence only allowing for reflection and preventing application of the theory to cases where transmission is important. In many situations, it is critical to consider two media and include the rough solid-solid interface between them, for instance in the study of the boundary phonon scattering/transport at the Si/Ge interface commonly seen for a phonon device [8]. The physics of solid-solid rough interface scattering can be very different from that of a single medium with a stress-free boundary condition. For instance, a considerable portion of incident energy can be transmitted through the interface, and the roughness could be expected to have different effects on the reflection and transmission depending on the materials; even the reflection itself would be different from that with a stress-free rough surface.

This article is organized as follows. Section II describes the derivation of the theoretical formulas representing the diffuse scattering field using the KA. Numerical simulations are performed in Sec. III to explore the accuracy of the derived expressions. Section IV illustrates effects of roughness and material properties on the diffuse field, for different modes. Section V discusses implications for phonon boundary scattering. Finally, we draw together concluding remarks in Sec. V.

II. THEORETICAL FORMULAS WITH KIRCHOFF APPROXIMATION

The scattering system in two dimensions (2D) is shown in Fig. 1, with a rough interface, separating two elastic solids, insonified by an incident P wave from Solid 1. A fraction of the elastic waves transmit through the interface to Solid 2, while the rest are reflected back into Solid 1. The unit incident and scattering vectors for P or mode-converted S waves are denoted as:

$$\hat{\boldsymbol{k}}_{\boldsymbol{in}} = (\sin\theta_i, -\cos\theta_i)$$
$$\hat{\boldsymbol{k}}_{\boldsymbol{sc}} = \begin{cases} (\sin\theta_s, \cos\theta_s), & \text{reflection} \\ (\sin\theta_s, -\cos\theta_s), & \text{transmission}, \end{cases} \tag{2}$$

where θ_i and θ_s refer to the incidence and scattering angles with respect to the normal of the surface mean plane.

The rms value σ of $h(x_1)$ is normally used as a measure of the height scale of the surface. Besides, the lateral variation of $h(x_1)$ is characterized by the correlation function, and it is assumed to be a Gaussian in this article [1]:

$$W(\Delta x_1) = \frac{\langle h(x_1)h(x_1+\Delta x_1)\rangle}{\sigma^2} = \exp\left(-\frac{\Delta x_1^2}{\lambda_0^2}\right), \tag{3}$$

where λ_0 is called the correlation length, as the distance over which the correlation function falls by $1/e$.

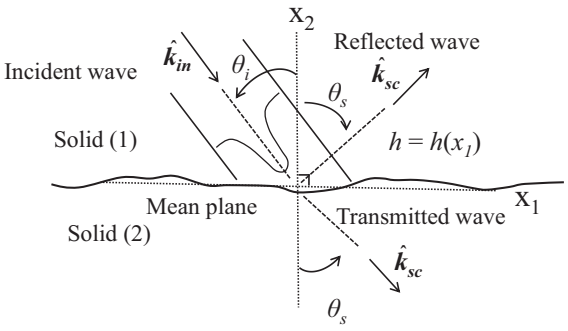

FIG. 1. Sketch for an incident Gaussian beam (P wave) scattered from a 1D rough interface separating two elastic solids.

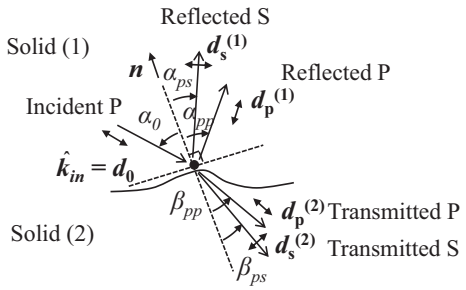

FIG. 2. Illustration of the elastodynamic Kirchhoff approximation.

A. Kirchhoff theory

We assume linear, isotropic and homogeneous elastic media as described in textbooks in continuum mechanics [27–29] among many others, and draw in particular on Ref. [29]. The elastodynamic KA is illustrated in Fig. 2 at one local surface point, insonified by a P wave. The KA assumes that the motion of this local point is the same as if it were part of an infinite tangential plane insonified by the incident wave [1]. Physically this has an implicit limitation to having the correlation length greater than the wavelength and furthermore, in this limit, the excitation of Rayleigh surface waves will not be relevant, as an incident plane wave on a flat surface does not generate Rayleigh waves. In calculations where the correlation length is allowed to vary [10], the Rayleigh wave contribution only becomes noticeable for small correlation lengths.

Following the continuity of displacement and traction on the interface, the total surface displacement and traction are expressed as the summation of the incident and reflection fields, which also equals those of the transmission field:

$$\begin{aligned} \boldsymbol{u} &= \boldsymbol{d}_0 + R_{pp}\boldsymbol{d}_p^{(1)} + R_{ps}\boldsymbol{d}_s^{(1)} = D_{pp}\boldsymbol{d}_p^{(2)} + D_{ps}\boldsymbol{d}_s^{(2)} \\ \boldsymbol{t} &= \boldsymbol{t}_0 + \boldsymbol{t}_p^{(1)} + \boldsymbol{t}_s^{(1)} = \boldsymbol{t}_p^{(2)} + \boldsymbol{t}_s^{(2)}, \end{aligned} \tag{4}$$

where $\boldsymbol{u}$ and $\boldsymbol{t}$ are the displacements and tractions respectively and R_{pp}, R_{ps}, D_{pp}, and D_{ps} are the Fresnel reflection and transmission coefficients of P and mode-converted S waves respectively [29]. The $\boldsymbol{d}_0$, $\boldsymbol{d}_p^{(1)}$, $\boldsymbol{d}_s^{(1)}$, $\boldsymbol{d}_p^{(2)}$, and $\boldsymbol{d}_s^{(2)}$ are the displacement polarization vectors for the incident P, reflected, and transmitted P/S waves, as shown in Fig. 2, and the corresponding tractions from incident and reflected/transmitted waves are denoted as $\boldsymbol{t}_0$, $\boldsymbol{t}_p^{(1)}$, $\boldsymbol{t}_s^{(1)}$, $\boldsymbol{t}_p^{(2)}$, and $\boldsymbol{t}_s^{(2)}$. These values of tractions are obtained from the displacement field according to Hooke's law and the stress-strain relationship. In Fig. 2, the local incident/scattering angles with respect to the normal of the tangential plane are denoted as α_0, α_{pp}, α_{ps}, β_{pp}, and β_{ps}, and they obey the Snell's law.

By moving $\boldsymbol{d}_0$ and $\boldsymbol{t}_0$ to one side of Eq. (4) respectively, Eq. (4) is conveniently recast as a matrix equation:

$$\begin{aligned} \mathbf{M}\boldsymbol{X} &= \boldsymbol{b} \\ \boldsymbol{X} &= [R_{pp}\ \ R_{ps}\ \ D_{pp}\ \ D_{ps}]^T, \end{aligned} \tag{5}$$

where $\mathbf{M}$ is a 4×4 matrix, and $\boldsymbol{b}$ is a 4×1 vector representing the incident field. For the case with an incident P wave, the expressions of $\mathbf{M}$ and $\boldsymbol{b}$ are:

$$\mathbf{M} = \begin{bmatrix} -\cos\alpha_{pp} & \sin\alpha_{ps} & -\cos\beta_{pp} & \sin\beta_{ps} \\ -\sin\alpha_{pp} & -\cos\alpha_{ps} & \sin\beta_{pp} & \cos\beta_{ps} \\ -\cos 2\alpha_{ps} & \frac{c_s^{(1)}}{c_p^{(1)}}\sin 2\alpha_{ps} & \frac{\rho^{(2)}}{\rho^{(1)}}\frac{c_p^{(2)}}{c_p^{(1)}}\cos 2\beta_{ps} & -\frac{\rho^{(2)}}{\rho^{(1)}}\frac{c_s^{(2)}}{c_p^{(1)}}\sin 2\beta_{ps} \\ -\sin 2\alpha_{pp} & \frac{c_p^{(1)}}{c_s^{(1)}}\cos 2\alpha_{ps} & \frac{\rho^{(2)}}{\rho^{(1)}}\frac{c_p^{(1)}}{c_p^{(2)}}\left(\frac{c_s^{(2)}}{c_s^{(1)}}\right)^2\sin 2\beta_{pp} & -\frac{\rho^{(2)}}{\rho^{(1)}}\frac{c_s^{(2)}}{c_s^{(1)}}\frac{c_p^{(1)}}{c_s^{(1)}}\cos 2\beta_{ps} \end{bmatrix} \tag{6}$$

and

$$\boldsymbol{b} = [-\cos\alpha_0\ \ \sin\alpha_0\ \ \cos 2\alpha_{ps}\ \ -\sin 2\alpha_0]^T, \tag{7}$$

where $\rho^{(1)}$ and $\rho^{(2)}$ refer to the density of Solid 1 and Solid 2. $c_p^{(1)}$, $c_s^{(1)}$, $c_p^{(2)}$, and $c_s^{(2)}$ are compressional or shear wave speed in Solid 1 or 2. By solving for $\boldsymbol{X}$ in the linear system of Eq. (5), one obtains the Fresnel reflection/transmission coefficients, which are position-dependent along the interface; the total displacement $\boldsymbol{u}$ and subsequently the traction $\boldsymbol{t}$ at one surface point can then be calculated by substituting the solved Fresnel coefficients into Eq. (4).

The elastodynamic Helmholtz integral formula [29] with the integral taken along the rough interface $\mathcal{S}$:

$$\begin{aligned} u_k(\boldsymbol{r}) = \int_{\mathcal{S}} &\left[\sigma_{ij;k}^G(|\boldsymbol{r}-\boldsymbol{r}_0|)u_i(\boldsymbol{r}_0)n_j(\boldsymbol{r}_0)\right. \\ &\left. - \sigma_{ij}(\boldsymbol{r}_0)u_{i;k}^G(|\boldsymbol{r}-\boldsymbol{r}_0|)n_j(\boldsymbol{r}_0)\right] dS(\boldsymbol{r}_0) \\ &\times \text{where } i,j,k = 1,2 \end{aligned} \tag{8}$$

is key and is used to calculate the scattered displacement $u_k(\boldsymbol{r})$ where $\boldsymbol{r}$ is the vector indicating the position of the observation point, and n_j is the unit normal vector pointing outside the surface. In Eq. (8) $u_i(\boldsymbol{r}_0)$ and $\sigma_{ij}(\boldsymbol{r}_0)$ represent the displacement and stress at a point $\boldsymbol{r}_0$ on the interface; also required are the elastodynamic Green's functions in the unbounded domain $u_{i;k}^G(|\boldsymbol{r}-\boldsymbol{r}_0|)$ and $\sigma_{ij;k}^G(|\boldsymbol{r}-\boldsymbol{r}_0|)$. The Green's function can be expressed explicitly as [29]:

$$\begin{aligned} u_{i;k}^G(|\boldsymbol{r}-\boldsymbol{r}_0|) &= \frac{1}{\mu k_s^2}[-G(k_p|\boldsymbol{r}-\boldsymbol{r}_0|) + G(k_s|\boldsymbol{r}-\boldsymbol{r}_0|)]_{,ik} \\ &\quad + G(k_s|\boldsymbol{r}-\boldsymbol{r}_0|)\delta_{ik} \\ \sigma_{ij;k}^G(|\boldsymbol{r}-\boldsymbol{r}_0|) &= \left(1 - 2k_p^2/k_s^2\right)G(k_p|\boldsymbol{r}-\boldsymbol{r}_0|)_{,k}\delta_{ij} \\ &\quad - \frac{2}{k_s^2}[G(k_p|\boldsymbol{r}-\boldsymbol{r}_0|) - G(k_s|\boldsymbol{r}-\boldsymbol{r}_0|)]_{,ijk} \\ &\quad + G(k_s|\boldsymbol{r}-\boldsymbol{r}_0|)_{,j}\delta_{ik} + G(k_s|\boldsymbol{r}-\boldsymbol{r}_0|)_{,i}\delta_{jk}, \end{aligned} \tag{9}$$

where k_p and k_s are the compressional and shear wave number, and μ is the Lamé second parameter. The notation $f_{,i} = \frac{\partial f}{\partial x_i}$ is used here, and δ refers to the Dirac δ function. The function $G(k_\beta|\boldsymbol{r}-\boldsymbol{r}_0|)$ is the acoustic Green's function, which in 2D is expressed as:

$$G(k_\beta|\boldsymbol{r}-\boldsymbol{r}_0|) = -\frac{i}{4}H_0^{(1)}(k_\beta|\boldsymbol{r}-\boldsymbol{r}_0|). \tag{10}$$

Here $H_0^{(1)}(k_\beta|\boldsymbol{r}-\boldsymbol{r}_0|)$ denotes the zero order Hankel function of the first kind.

Our interest is in the far field and so we take the far field approximation that $|\boldsymbol{r}-\boldsymbol{r_0}| \approx r - \hat{\boldsymbol{r}}\cdot\boldsymbol{r_0}$, and the Hankel function can be approximated as:

$$H_0^{(1)}(k_\beta|\boldsymbol{r}-\boldsymbol{r}_0|) \approx \left(\frac{2}{\pi k_\beta}\right)^{1/2} e^{-i\pi/4}(e^{ik_\beta r}/\sqrt{r})e^{-ik_\beta\hat{\boldsymbol{r}}\cdot\boldsymbol{r_0}}. \tag{11}$$

In 2D Eq. (8) is then transferred into an integral along the mean plane of the surface $\mathcal{S}_m$:

$$\boldsymbol{u}_\beta(\boldsymbol{r}) = -ik_\beta\sqrt{\frac{2\pi i}{k_\beta}}\frac{\exp(ik_\beta r)}{4\pi\sqrt{r}}\int_{\mathcal{S}_m}\left(\boldsymbol{U}_\beta + \frac{\boldsymbol{T}_\beta}{ik_\beta\rho c_\beta^2}\right) \times \exp(ik_\beta\phi_\beta)d\mathcal{S}_m \quad \beta = p,s, \tag{12}$$

where k_β and c_β refer to the wave number and wave speed of the scattered waves, and ρ is the density. They are different for Solid 1 (reflection) and Solid 2 (transmission). The phase term $\phi_\beta = A_\beta x_1 + C_\beta h(x_1)$, and

$$A_\beta = \frac{k_p^{(1)}}{k_\beta}\sin\theta_i - \sin\theta_s$$
$$C_\beta = \begin{cases} -\left(\frac{k_p^{(1)}}{k_\beta^{(1)}}\cos\theta_i + \cos\theta_s\right), & \text{reflection} \\ -\left(\frac{k_p^{(1)}}{k_\beta^{(2)}}\cos\theta_i - \cos\theta_s\right), & \text{transmission} \end{cases}, \tag{13}$$

where $k_p^{(1)}$ stands for the wave number of the incident compressional waves from Solid 1. We emphasise that C_β has different expressions for reflection and transmission. The terms $\boldsymbol{U}_\beta$ and $\boldsymbol{T}_\beta$ represent the decomposed boundary displacement and traction for different wave modes and they are expressed as:

$$\boldsymbol{U}_p = \left[(\boldsymbol{u}\cdot\boldsymbol{N})\left(1-2\left(\frac{c_s}{c_p}\right)^2\right)+2\left(\frac{c_s}{c_p}\right)^2(\boldsymbol{u}\cdot\hat{\boldsymbol{k}}_{\boldsymbol{sc}})(\boldsymbol{N}\cdot\hat{\boldsymbol{k}}_{\boldsymbol{sc}})\right]\hat{\boldsymbol{k}}_{\boldsymbol{sc}}$$
$$\boldsymbol{U}_s = (\boldsymbol{N}\cdot\hat{\boldsymbol{k}}_{\boldsymbol{sc}})\boldsymbol{u} + (\boldsymbol{u}\cdot\hat{\boldsymbol{k}}_{\boldsymbol{sc}})\boldsymbol{N} - 2(\boldsymbol{u}\cdot\hat{\boldsymbol{k}}_{\boldsymbol{sc}})(\boldsymbol{N}\cdot\hat{\boldsymbol{k}}_{\boldsymbol{sc}})\hat{\boldsymbol{k}}_{\boldsymbol{sc}}$$
$$\boldsymbol{T}_p = (\hat{\boldsymbol{k}}_{\boldsymbol{sc}}\cdot\boldsymbol{t})\hat{\boldsymbol{k}}_{\boldsymbol{sc}}$$
$$\boldsymbol{T}_s = \boldsymbol{t} - (\hat{\boldsymbol{k}}_{\boldsymbol{sc}}\cdot\boldsymbol{t})\hat{\boldsymbol{k}}_{\boldsymbol{sc}} \tag{14}$$

in which $\boldsymbol{N}$ is the unnormalized vector normal to the surface, and it equals $(-\partial h/\partial x_1, 1)$. The interface displacement $\boldsymbol{u}$ and traction $\boldsymbol{t}$ are obtained using the KA from Eqs. (4)–(7). We assume an incident P wave in this article, and hence neglect the subscript α denoting the incident mode. Note that the same methodology can be equivalently applied to an incident S wave. For shear wave incidence, one needs to revise Eq. (4)–(7) to calculate the Fresnel reflection/transmission coefficients representing a plane S wave reflected from the tangential plane.

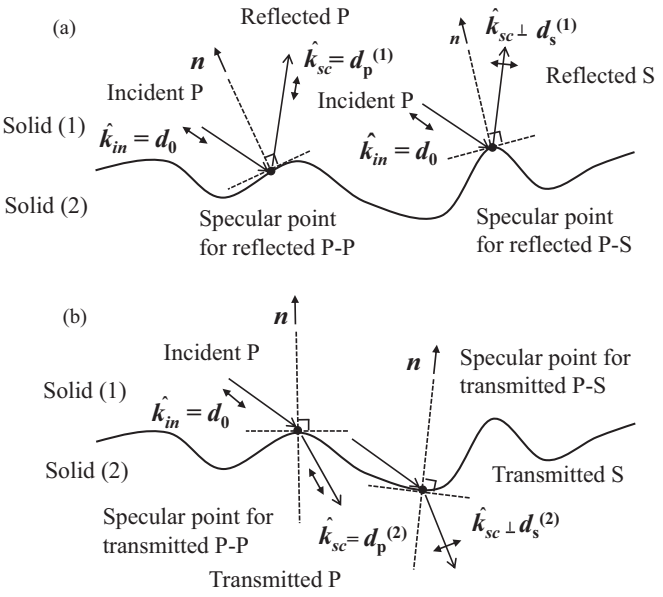

FIG. 3. Specular points for different modes. (a) Reflection P-P and P-S modes. (b) Transmission P-P and P-S modes.

It is necessary to remove the surface slope from the integration in Eq. (12), for the analytical derivation of the ensemble averaging $\langle u_k\bar{u}_j\rangle$ later (the overline denoting the complex conjugate). Following the method described in Ref. [5], we apply a stationary phase approach to Eq. (12) to approximate $\boldsymbol{U}_\beta$ and $\boldsymbol{T}_\beta$. The first-order derivatives of the phase term ϕ_β with respect to x_1 is set to be zero to locate the stationary phase points, and the following expression is obtained:

$$\frac{\partial h}{\partial x_1} = -\frac{A_\beta}{C_\beta}. \tag{15}$$

The underlying physics of this is that the varying slope along the surface is approximated as constant for given incidence/scattering angles, wave modes, and material properties; the stationary phase points are also called specular points in the optical community [30]. At these points, the scattering direction is viewed the same as the specular direction (reflection or transmission) to the incidence angle with respect to the local normal vector, as illustrated in Fig. 3 for both the reflection and transmission modes. The boundary integral Eq. (12) is therefore dominated by contributions from these points where the phase term ϕ_β is stationary.

By substituting the slope approximation in Eq. (15) into Eqs. (12)–(14), the values of $\boldsymbol{U}_\beta$ and $\boldsymbol{T}_\beta$ at the specular points are calculated. Here we assume that

$$\boldsymbol{F}_\beta = 1/2\left(\boldsymbol{U}_\beta + \frac{\boldsymbol{T}_\beta}{ik_\beta\rho c_\beta^2}\right),$$

which is called the elastodynamic angular factor hereinafter. The function $\boldsymbol{F}_\beta$ depends on the incidence/scattering angle, material properties in both media and wave modes, and it is a vector containing two components corresponding to the polarization of the displacement. By eliminating the

dependence of the surface gradient, Eq. (12) is simplified as:

$$\boldsymbol{u}_\beta(\boldsymbol{R}) = -ik_\beta\sqrt{\frac{2\pi i}{k_\beta}}\frac{\exp(ik_\beta r)}{4\pi\sqrt{r}}2\boldsymbol{F_\beta}\int_{\mathcal{S}_m}\exp(ik_\beta\phi_\beta)d\mathcal{S}. \tag{16}$$

B. Expected scattering cross section

We are now in a position to derive the expression for the scattering cross section, an important normalized metric commonly used. The expected scattering cross section ($\langle\sigma_{sc,\beta}\rangle$) for waves scattered from a rough surface is expressed as [29]:

$$\langle\sigma_{sc,\beta}\rangle = \frac{r\langle\boldsymbol{P}_{sc,\beta}\cdot\hat{\boldsymbol{k}}_{\boldsymbol{sc}}\rangle}{E_{\text{inc}}}, \tag{17}$$

where $\langle\boldsymbol{P}_{sc,\beta}\cdot\hat{\boldsymbol{k}}_{\boldsymbol{sc}}\rangle$ is the scattering power flux per unit area of the plane perpendicular to the scattering vector. E_{inc} refers to the incident energy, which equals the incident power flux $\boldsymbol{P}_{\text{inc}}$ integrated over the surface mean plane, and it is expressed as:

$$E_{\text{inc}} = \int_{-\infty}^{\infty}\boldsymbol{P}_{\text{inc}}\cdot\hat{\boldsymbol{x}}_{\boldsymbol{2}}dx_1, \tag{18}$$

where $\hat{\boldsymbol{x}}_{\boldsymbol{2}}$ denotes the unit vector in the x_2 direction normal to the surface. The ith component of the power flux P is defined as:

$$\begin{aligned}\langle P_i\rangle &= \left\langle\tau_{ij}\frac{\partial u_j}{\partial t}\right\rangle \\ &= -i\omega[\lambda ik_q\langle u_q\bar{u}_j\rangle\delta_{ij} + \mu(ik_j\langle u_i\bar{u}_j\rangle + ik_i\langle u_j\bar{u}_j\rangle)],\end{aligned} \tag{19}$$

where τ_{ij} is the stress, k_i is the ith component of the wave vector, u_i is the displacement and $\bar{u}_i$ is its conjugate value. λ and μ are Lamé first and second parameters, which are different for Solid 1 and Solid 2.

The displacement of the incident wave is assumed to be a Gaussian tapered plane wave with the form given as [31]:

$$\begin{aligned}\boldsymbol{\Psi}(x_1,x_2) &= \boldsymbol{d}_0\exp\left\{ik_p^{(1)}(x_1\sin\theta_0 - x_2\cos\theta_0)[1+\eta(x_1,x_2)]\right. \\ &\quad\left.-[(x_1\cos\theta_0 + x_2\sin\theta_0)/w]^2\right\} \\ \eta(x_1,x_2) &= \frac{c_p^{(1)2}}{\omega^2w^2}\left[\frac{2}{w^2}(x_1\cos\theta_0 + x_2\sin\theta_0)^2 - 1\right],\end{aligned} \tag{20}$$

where w is the half-width of the Gaussian beam, at which the value of the incident amplitude falls by $1/e$. $c_p^{(1)}$ and $k_p^{(1)}$ are the compressional wave speed and wave number in Solid 1. By substituting Eq. (20) into Eqs. (19), (18), the incident energy E_{inc} through the mean surface plane has been derived by [31]:

$$\begin{aligned}E_{\text{inc}} &= \frac{\sqrt{\pi}w\omega^2}{\sqrt{2}c_p^{(1)}}P_B \\ P_B &= \left[1 - \frac{c_p^{(1)2}}{\omega^2w^2}(1+2\tan^2\theta_0)\right][(\lambda^{(1)}+2\mu^{(1)})\cos^2\theta_0 \\ &\quad+\mu^{(1)}\sin^2\theta_0] \\ &\quad+\left[\left(1+\frac{1}{2}\frac{c_p^{(1)2}}{w^2\omega^2}\right)\tan\theta_0\right](\lambda^{(1)}+\mu^{(1)})\sin\theta_0\cos\theta_0.\end{aligned} \tag{21}$$

From Eqs. (17) to (19), the calculation of the ensemble averaging $\langle\sigma_{sc,\beta}\rangle$ is reduced to deriving the expression for $\langle u_i\bar{u}_j\rangle$. According to Eq. (16), $\langle u_i\bar{u}_j\rangle$ of the scattered waves is:

$$\begin{aligned}\langle u_i\bar{u}_j\rangle &= \frac{k_\beta F_{i,\beta}F_{j,\beta}}{2\pi r}\int_{\mathcal{S}}\int_{\mathcal{S}}\Psi(x_1)\Psi(x_1')e^{ik_\beta A_\beta(x_1-x_1')} \\ &\quad\langle e^{ik_\beta C_\beta(h-h')}\rangle dx_1dx_1',\end{aligned} \tag{22}$$

where the function $\Psi(x_1)$ represents the incident displacement field along the mean surface calculated from the Gaussian tapered plane wave in Eq. (20). Following the derivation in [5], Eq. (22) is simplified via a change of variable that $\Delta x_1 = x_1' - x_1$

$$\begin{aligned}\langle u_i\bar{u}_j\rangle &= \frac{k_\beta F_{i,\beta}F_{j,\beta}}{2\pi r}\int_{-\infty}^{\infty}\int_{-\infty}^{\infty}\Psi(x_1)\Psi(\Delta x_1+x_1)dx_1 \\ &\quad\times e^{ik_\beta A_\beta\Delta x_1}\chi_2(k_\beta C_\beta,\Delta x_1)d\Delta x_1,\end{aligned} \tag{23}$$

where $\chi_2(k_\beta C_\beta,\Delta x_1)$ is called the two-dimensional characteristic function [1]. If the surface height follows the Gaussian distribution, $\chi_2(k_\beta C_\beta,\Delta x_1)$ then has an analytical form:

$$\chi_2(k_\beta C_\beta,\Delta x_1) = \exp\{-g_\beta[1-W(\Delta x_1)]\}, \tag{24}$$

where the parameter g_β is different from Eq. (1), as it includes both reflection and transmission, and nonspecular angles:

$$\begin{aligned}g_\beta &= k_\beta^2C_\beta^2\sigma^2 \\ &= \begin{cases}\left(k_p^{(1)}\cos\theta_i + k_\beta^{(1)}\cos\theta_s\right)^2\sigma^2, & \text{reflection} \\ \left(k_p^{(1)}\cos\theta_i - k_\beta^{(2)}\cos\theta_s\right)^2\sigma^2, & \text{transmission}\end{cases}.\end{aligned} \tag{25}$$

Now assuming the first integral of $\Psi(x_1)\Psi(\Delta x_1+x_1)$ is a slowly varying function around the point $\Delta x_1 = 0$ as compared with $\chi_2(k_\beta C_\beta,\Delta x_1)$; this is accurate provided the half-width of the beam w is larger than $3\lambda_p$. Equation (23) is then further simplified as:

$$\begin{aligned}\langle u_i\bar{u}_j\rangle &\approx \frac{k_\beta F_{i,\beta}F_{j,\beta}}{2\pi r}\int_{-\infty}^{\infty}\Psi(x_1)^2dx_1\int_{-\infty}^{\infty}e^{ik_\beta A_\beta\Delta x_1} \\ &\quad\times\chi_2(k_\beta C_\beta,\Delta x_1)d\Delta x_1 \\ &= \frac{k_\beta F_{i,\beta}F_{j,\beta}}{2\pi r}L_{\text{eff}}\Sigma_{n=0}^{\infty}e^{-g_\beta}\frac{g_\beta^n}{n!}\int_{-\infty}^{\infty}e^{ik_\beta A_\beta\Delta x_1} \\ &\quad\times W^n(\Delta x_1)d\Delta x_1.\end{aligned} \tag{26}$$

Here the parameter $L_{\text{eff}} = \int_{-\infty}^{\infty}\Psi^2(x_1)dx_1$, is the effective insonified length. We now identify the coherent and diffuse contributions: the first term in Eq. (26) when $n=0$ corresponds to the coherent component, while the diffuse field contribution comes from higher-order terms. Substituting the Gaussian correlation function Eq. (3) into Eq. (26), the diffuse components of $\langle u_i\bar{u}_j\rangle$ are expressed as:

$$\begin{aligned}\langle u_i\bar{u}_j\rangle^d &= \frac{k_\beta F_{i,\beta}F_{j,\beta}\lambda_0\sqrt{\pi}e^{-g_\beta}}{2\pi r}L_{\text{eff}}\Sigma_{n=1}^{\infty}\frac{g_\beta^n}{n!\sqrt{n}} \\ &\quad\times\exp\left[-\frac{k_\beta^2A_\beta^2\lambda_0^2}{4n}\right].\end{aligned} \tag{27}$$

In the low-frequency limit or when the rms value is very small compared with the wavelength, the scattering cross

section is approximated by only keeping the first term of the Taylor series in Eq. (27) [1]:

$$\langle u_i \bar{u}_j \rangle^d \approx \frac{k_\beta F_{i,\beta} F_{j,\beta} \lambda_0 \sqrt{\pi} e^{-g_\beta}}{2\pi r} L_{\text{eff}} g_\beta \exp\left[-\frac{k_\beta^2 A_\beta^2 \lambda_0^2}{4}\right]$$
$$= \frac{k_\beta^3 F_{i,\beta} F_{j,\beta} e^{-g_\beta}}{r} C_\beta^2 L_{\text{eff}} P(k_\beta A_\beta), \quad (28)$$

where $P(k_\beta A_\beta)$ is called the power spectrum of the surface height [1].

In contrast to the low-frequency approximation, in the high-frequency limit when $k_\beta \to \infty$, we assume that $k_\beta C_\beta (h - h') \approx k_\beta C_\beta \frac{\partial h}{\partial x_1}$, and hence the ensemble averaging $\langle u_i \bar{u}_j \rangle$ is derived as:

$$\langle u_i \bar{u}_j \rangle^d \approx \frac{k_\beta F_{i,\beta} F_{j,\beta}}{2\pi r} L_{\text{eff}} \times \int_{-\infty}^{\infty} \left\langle e^{ik_\beta [(A_\beta + C_\beta \frac{\partial h}{\partial x}) \Delta x_1]} \right\rangle d\Delta x_1$$
$$= \frac{k_\beta F_{i,\beta} F_{j,\beta}}{2\pi r} L_{\text{eff}} \times \frac{2\pi}{k_\beta C_\beta} \left\langle \delta\left(\frac{\partial h}{\partial x} + \frac{A_\beta}{C_\beta},\right) \right\rangle$$
$$= \frac{F_{i,\beta} F_{j,\beta}}{r C_\beta} L_{\text{eff}} \int_{-\infty}^{\infty} p_g(\gamma_x) d\gamma_x \delta\left(\gamma_x + \frac{A_\beta}{C_\beta}\right)$$
$$= \frac{F_{i,\beta} F_{j,\beta}}{r C_\beta} L_{\text{eff}} \times p_g\left(\frac{\partial h}{\partial x} = -\frac{A_\beta}{C_\beta}\right), \quad (29)$$

where p_g is the probability function of the surface slope, defined as:

$$p_g\left(\frac{\partial h}{\partial x_1}\right) = \frac{\lambda_0}{2\sqrt{\pi}\sigma} \exp\left[-\frac{\left(\frac{\partial h}{\partial x_1}\right)^2 \lambda_0^2}{4\sigma^2}\right]. \quad (30)$$

The scattering cross section $\langle \sigma_{sc} \rangle$ is similarly decomposed into the coherent and the diffuse fields:

$$\langle \sigma_{sc} \rangle = \sigma_{sc}^c + \sigma_{sc}^d$$
$$= \sigma_{sc}^{\text{flat}} \exp(-g_\beta) + \sigma_{sc}^d. \quad (31)$$

The coherent scattering cross section is a simple exponential decay in terms of that from a flat surface. The diffuse scattering cross section σ_{sc}^d is obtained by substituting the expression of Eq. (27) into Eqs. (17)–(19).

III. NUMERICAL VERIFICATION

In this section, the predictions from the formulas for $\langle \sigma_{sc} \rangle$ are compared with full numerical Monte Carlo simulations; these simulations use Gaussian surfaces from low to high roughnesses ($\sigma = \lambda_p^{(1)}/20 \sim \lambda_p^{(1)}/2$, $\lambda_0 = 2\lambda_p^{(1)}, \lambda_p^{(1)}$ being the compressional wavelength in Solid 1). For each realization of the surface a purely numerical method, the finite element boundary integral (FEBI) approach [21,26], is performed to compute σ_{sc}. The FEBI method is highly efficient as it computes the very local scattering field on the interface using an explicit time domain FE scheme inside a small domain, and then performs a boundary integral to globally calculate the scattered waves. This approach significantly reduces the computational burden for rough surface calculations.

For the local FE computation, to yet further optimise the numerical simulations, we take advantage of the recently developed GPU driven FE software POGO [32] and this greatly accelerates the simulation. The local FE model also takes advantage of developments in absorbing regions [33] to prevent spurious reflections from the edges of the small computational domain from contaminating the results.

Figure 4 shows a snapshot from a typical local FE simulation of waves scattered from a rough interface. The two bulk media we take as example materials are silicon (Solid 1) and germanium (Solid 2), as they are typical media of interest, with densities and wave speeds of 2329 kg/m^3, 8320 m/s, and 5246 m/s for silicon and 5323 kg/m^3, 4866 m/s, and 2771 m/s for germanium. The FE model has a dimension of $37\lambda_p^{(1)} \times 10\lambda_p^{(1)}$, including an absorbing region [33] with a thickness of $3\lambda_p^{(1)}$. The rough interface separating two media has a length of $29\lambda_p^{(1)}$. A source line is placed $1.2\lambda_p^{(1)}$ above the rough interface on the Si side. It excites a Gaussian tapered plane P wave with a half beam width w of $5\lambda_p^{(1)}$ insonifying the interface, at an incidence angle of $\theta_i = 20°$; the use of the Gaussian tapered incident wave eliminates the edge effects [31]. The incident wave is assumed to be a five-cycle tone burst.

After computing the displacement and the stress on the interface, a boundary integral along the interface is performed to calculate the scattered waves. The FEBI method is run on each realization and the sample averaged scattering cross section from all realizations is then used to approximate the ensemble averaging against which we assess the accuracy of the analytical formulas. Specifically, surfaces with the same correlation length ($\lambda_0 = 2\lambda_p^{(1)}$), and rms values ranging from $\lambda_p^{(1)}/20$ to $\lambda_p^{(1)}/2$ are used to find the valid region of the analytical solution. For each roughness, 400 realizations of surfaces are generated [25] for simulations to obtain the mean scattering cross section.

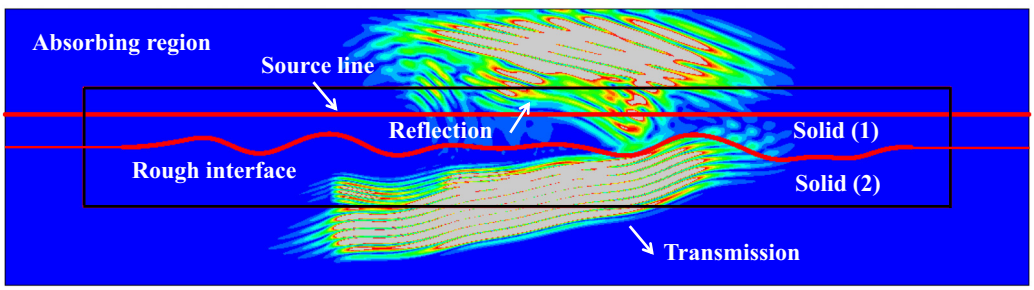

FIG. 4. Snapshot of animation in the local FE box showing the waves reflected and transmitted by the rough interface. Details of the simulation are given in the text.

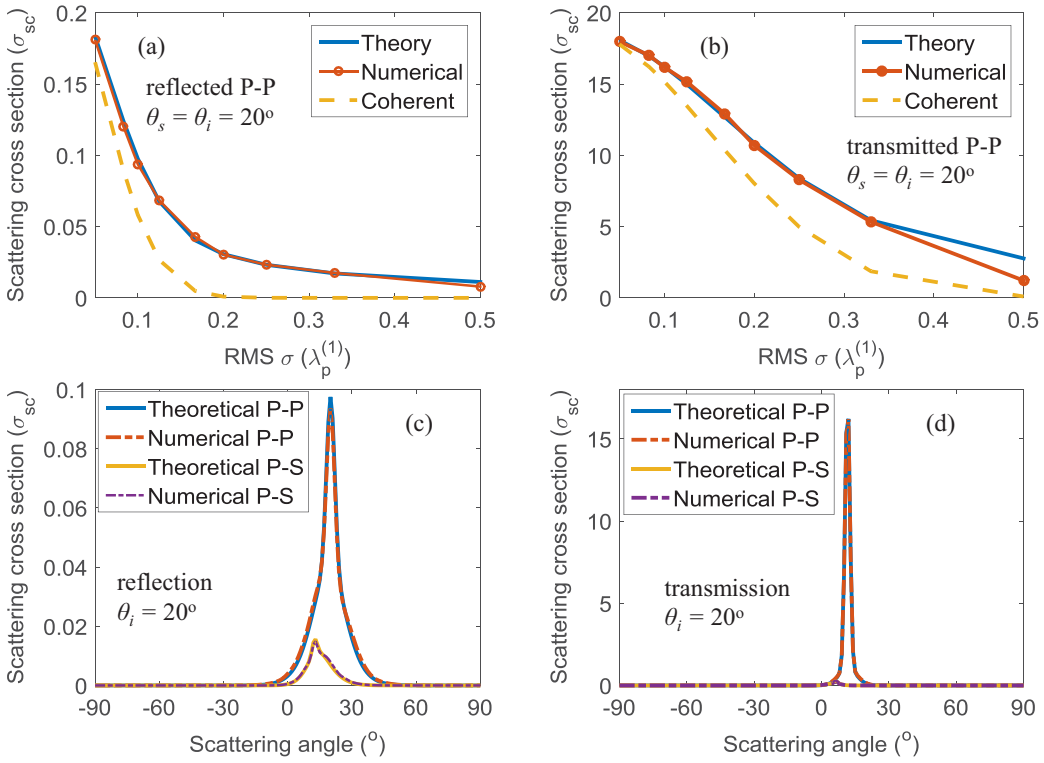

FIG. 5. Comparison of the theoretical results with those from numerical simulations ($\theta_i = 20^\circ$; Solid 1: Si; Solid 2: Ge). (a) Specular σ_{sc} of the reflected P-P mode. (b) Specular σ_{sc} of the transmitted P-P mode. (c) Angular distribution of σ_{sc} of the reflected P-P and P-S modes when $\sigma = \lambda_p^{(1)}/8$, $\lambda_0 = 2\lambda_p^{(1)}$. (d) Angular distribution of σ_{sc} of the transmitted P-P and P-S modes when $\sigma = \lambda_p^{(1)}/8$, $\lambda_0 = 2\lambda_p^{(1)}$.

Figures 5(a) and 5(b) show the total scattering cross sections (i.e., coherent + diffuse) for both the reflected P-P mode in Solid 1 and the transmitted P-P mode in Solid 2 at the specular angles as a function of σ. Note that according to Snell's law, the specular angle is 20° for the reflection and 11.5° for the transmission; the comparison shows an excellent match between the theoretical results and the sample averaged numerical results, when $\sigma \leqslant \lambda_p^{(1)}/2$, for both the reflection and transmission. The agreement indicates that the developed theoretical formulas using the Kirchhoff approximation is accurate for surfaces with a much wider range of roughness, as compared with the perturbation method [8]. In addition, the coherent scattering cross section predicted from the conventional Kirchhoff formula using Eq. (1) is plotted, and it is always below the numerical benchmark curve due to the lack of the diffuse component. It can also be observed that the transmission cross section attenuates with increasing roughness much more slowly than that for the reflection in the specular direction.

The angular distributions of $\langle\sigma_{sc}\rangle$ are plotted in Figs. 5(c) and 5(d) for both the reflection and transmission when $\sigma = \lambda_p^{(1)}/8$. The theoretical results again match very well with those computed from numerical simulations for both P-P and P-S modes, over a wide range of scattering angles. At grazing angles ($|\theta_s| \geqslant 70^\circ$), the Kirchhoff approximation is not reliable according to previous studies [25,26]; here the errors at these angles are not clearly seen in Figs. 5(c) and 5(d), due to the very small values of $\langle\sigma_{sc}\rangle$. Clear peaks at specular angles for different modes are found corresponding to the strong coherent field. In particular, the coherent peak is more dominant for the transmitted P-P mode in Fig. 5(d), than for the reflection in Fig. 5(c).

According to Eq. (13), the value of C_β is expressed differently depending on whether it is a reflection or a transmission event. This difference of C_β results in the divergence of the parameter g_β in Eq. (25), which determines the attenuation rate of the coherent field in terms of the roughness. For the Si/Ge interface simulated here, g_β for the transmission is smaller than that for the reflection, hence contributing to a much slower attenuation of the coherent field for the transmission. Therefore, a more noticeable peak is seen in Fig. 5(d), indicating that the coherent effects dictate the transmission. Similar conclusions are found for waves incident from liquid to solid using the phase screen method to model the coherent field [34]. Note that opposite situations exist where the transmitted coherent field decays quicker than the reflection. Such cases occur when g_β for the transmission is larger than the value for the reflection in the specular direction in Eq. (25), indicating waves impinging from a hard material to a comparably very soft material. In addition, the divergence of C_β in Eq. (13) also contributes to different behavior of the reflected and transmitted diffuse field, which will be shown in the next section.

IV. PHYSICAL ANALYSIS OF THE DIFFUSE FIELD

A. Angular distribution

The scattering patterns of the diffuse field when a P wave is incident at 20° from the side of Solid 1(Si) are

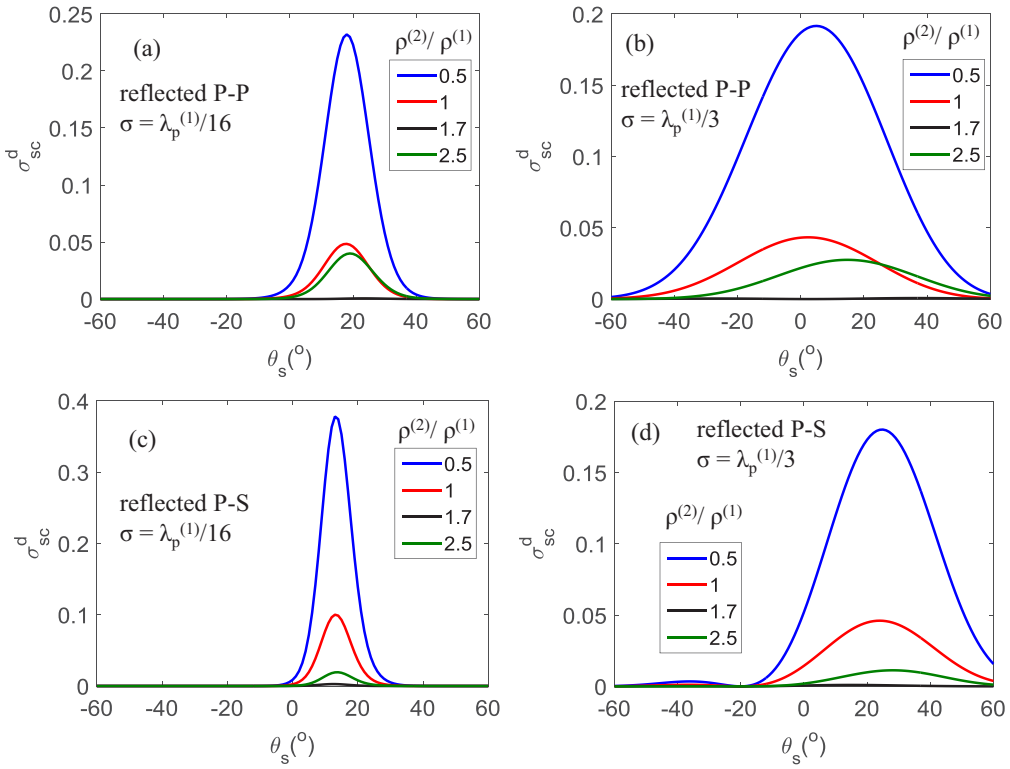

FIG. 6. Diffuse scattering cross section (σ^d_{sc}, reflection) from rough interfaces (Solid 1 is Si; Solid 2 has the same wave speed as Ge but various values of the density.) by a 20° incident P wave as a function of scattering angles. (a) Reflected P-P mode, $\sigma = \lambda_p^{(1)}/16$. (b) Reflected P-P mode, $\sigma = \lambda_p^{(1)}/3$. (c) Reflected P-S mode, $\sigma = \lambda_p^{(1)}/16$. (d) Reflected P-S mode, $\sigma = \lambda_p^{(1)}/3$. The correlation length $\lambda_0 = 2\lambda_p^{(1)}$.

shown in Fig. 6 for reflection and Fig. 7 for transmission. To explore the effect of material variation, Solid 2 is assumed to have the same wave speed as Ge, but with various values of the density (hence altering the elastic wave impedance); by changing the density, while keeping the wave speed of Solid 2, we are implicitly changing the Young's modulus. In each figure, we show results from a low ($\sigma = \lambda_p^{(1)}/16$) and a high roughness ($\sigma = \lambda_p^{(1)}/3$) case. The correlation length is assumed to be $\lambda_0 = 2\lambda_p^{(1)}$ for both cases. As seen in Figs. 6, 7, altering the density mainly changes the amplitude of σ^d_{sc} for both reflected and transmitted waves, while having limited influence on the overall shape of the scattering pattern. From Eq. (27) we know that varying the density only affects the angular factor $\boldsymbol{F}_\beta$, and hence it weakly affects the shape of scattering patterns. A perfect match of the compressional wave impedance of the two solids (e.g., $\rho^{(2)}/\rho^{(1)} = 1.7$) results in a zero reflection of the P-P mode denoted as the black curve in Figs. 6(a) and 6(b), and correspondingly a maximum transmission amplitude in Figs. 7(a) and 7(b). In addition, the peaks of the scattering patterns in the low-roughness cases are all located in the specular angles. This is because, in the small-roughness approximation, the peak of the scattering pattern occurs when A_β is zero from Eq. (28), corresponding to the specular angle.

The diffuse energy rises as the rms value increases from $\lambda_p^{(1)}/10$ to $\lambda_p^{(1)}/3$, altering the scattering patterns as shown in Figs. 6 and 7; the effect of the roughness is different depending on whether reflection and transmission is considered. In general the diffuse energy becomes more widely spread, and this trend is more apparent for the reflection than the transmission. In addition, the peaks of the reflection patterns are moving away from the specular direction in Fig. 6, while these peaks almost stay around the specular direction for the transmission shown in Fig. 7, especially for the transmitted P-P mode. The different behavior of the reflection and transmission patterns is explained using the high-frequency asymptotic solution in Eq. (29). Recall that the specular points for the reflection differ from those for the transmission as shown in Fig. 2, corresponding to different values of the surface slopes ($\partial h/\partial x_1 = -A_\beta/C_\beta$). For the Si/Ge interface analysed here, the probability function $p_g(\partial h/\partial x_1)$ evaluated at the specular points for the transmission has a much narrower angular distribution around the specular direction than it does for the reflection. As a consequence, the shape and also the peaks of the transmission pattern appear to be weakly affected by increasing σ, although the amplitude has been significantly changed.

We also investigate cases where we vary the wave speed ($c_p^{(2)}$) of Solid 2 as shown in Fig. 8, while the density of Solid 2 is the same as Ge. Both the amplitude and the shape of the scattering pattern for the P-P mode are affected by the change of $c_p^{(2)}$, which is more apparent for the transmission case. It is also noticeable that the diffuse field for the transmitted P-P mode vanishes when $c_p^{(1)} = c_p^{(2)}$ as shown in Fig. 8(c). At this specific ratio of wave speed, from Eq. (13) we know that the parameter C_β for the transmitted P-P mode is zero at the specular direction; the exponential decaying factor g_β becomes zero from Eq. (25), indicating that the transmission is completely occupied by the same coherent effect as that from a flat surface. Therefore the diffuse field for the transmission

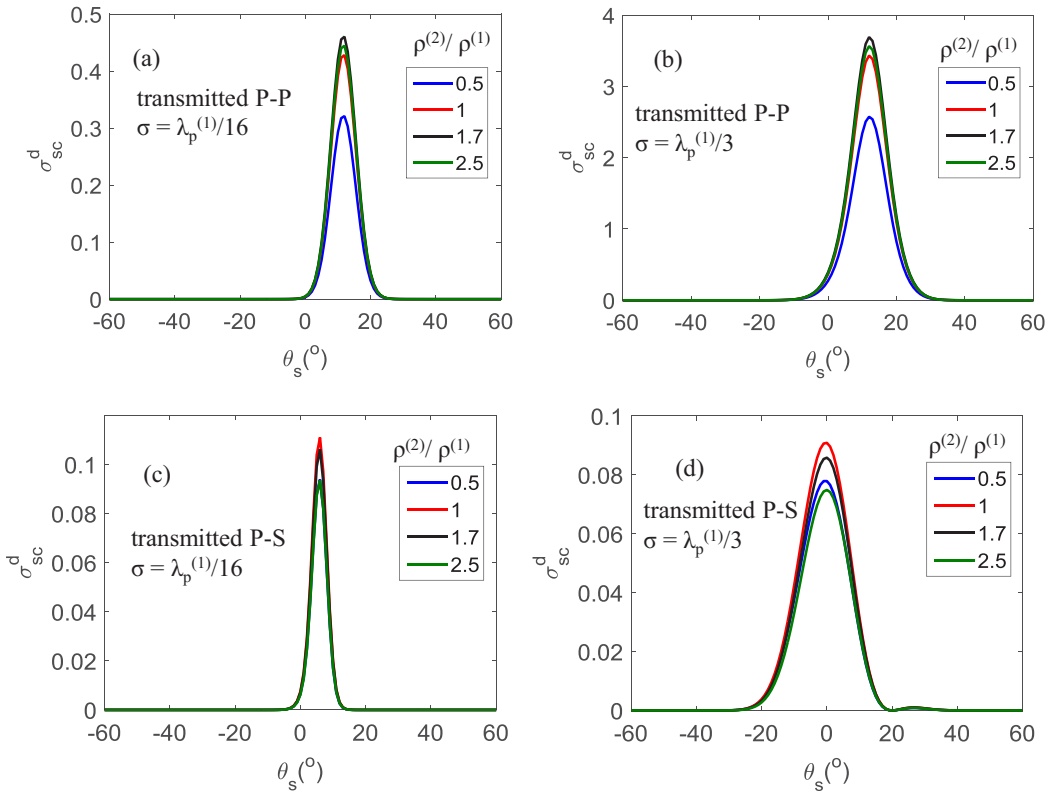

FIG. 7. Diffuse scattering cross section (σ_{sc}^{d}, transmission) from rough interfaces (Solid 1 is Si; Solid 2 has the same wave speed as Ge but various values of the density) by a 20° incident P wave as a function of scattering angles (θ_s). (a) Transmitted P-P mode, $\sigma = \lambda_p^{(1)}/16$. (b) Transmitted P-P mode, $\sigma = \lambda_p^{(1)}/3$. (c) Transmitted P-S mode, $\sigma = \lambda_p^{(1)}/16$. (d) Transmitted P-S mode, $\sigma = \lambda_p^{(1)}/3$. The correlation length $\lambda_0 = 2\lambda_p^{(1)}$.

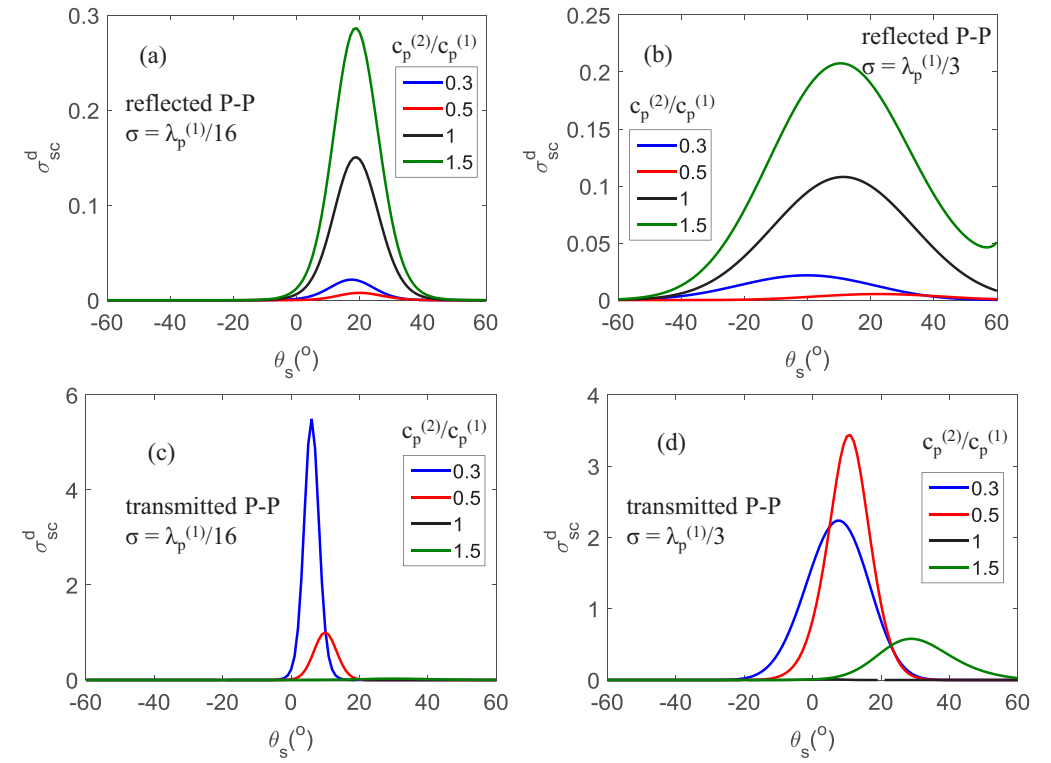

FIG. 8. Diffuse scattering cross section (σ_{sc}^{d}) from rough interfaces (Solid 1 is Si; Solid 2 has the same density as Ge but various values of the wave speed) by a 20° incident P wave as a function of scattering angles. (a) Reflected P-P mode, $\sigma = \lambda_p^{(1)}/16$. (b) Reflected P-P mode, $\sigma = \lambda_p^{(1)}/3$. (c) Transmitted P-P mode, $\sigma = \lambda_p^{(1)}/16$. (d) Transmitted P-P mode, $\sigma = \lambda_p^{(1)}/3$. The correlation length $\lambda_0 = 2\lambda_p^{(1)}$.

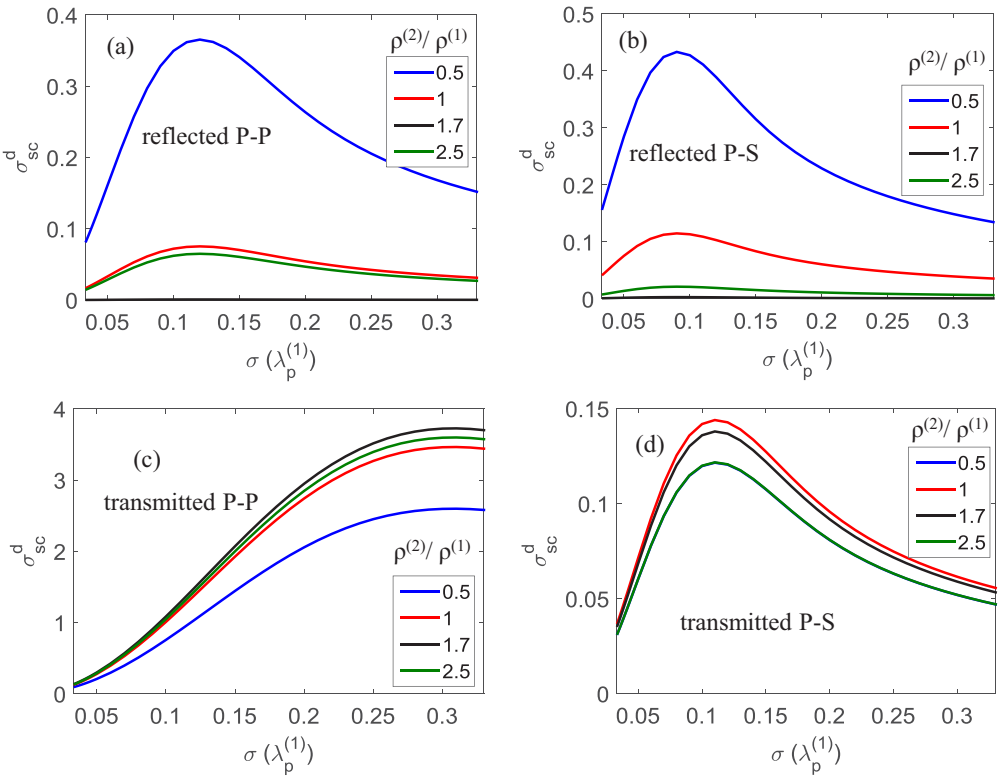

FIG. 9. Diffuse scattering cross section (σ^d_{sc}) at the specular direction from an interface (Solid 1 is Si; Solid 2 has the same wave speed as Ge but various values of the density) by a 20° incident P wave as a function of rms values (σ) when the correlation length $\lambda_0 = 2\lambda_p^{(1)}$. (a) Reflected P-P. (b) Reflected P-S. (c) Transmitted P-P. (d) Transmitted P-S.

vanishes when $c_p^{(1)} = c_p^{(2)}$, in other words, the waves travel through the interface as if the roughness did not exist if there is a perfect match of the wave speed.

B. Specular scattering

In many applications specific interest focuses on the interface scattering around the specular direction. For example, in the study of the phonon transport the specularity is a key parameter to calculate the thermal conductivity [9,10]. Figure 9 shows the specular scattering cross section $\langle\sigma^d_{sc}\rangle$ as a function of σ when varying the density $\rho^{(2)}$. Clear peaks are observed at intermediate values of roughness σ_{med}, and for each mode the locations of these peaks are independent of the density $\rho^{(2)}$. It is noticeable that the peak for the transmitted P-P mode appears at a much higher roughness ($\sigma = \lambda_p^{(1)}/4$) than for other modes ($\sigma = \lambda_p^{(1)}/8$).

To understand σ_{med} and the corresponding peaks, the Rayleigh parameter is quoted here [1]:

$$R_a = \frac{\sqrt{g_\beta}}{2}, \tag{32}$$

where g_β is from Eq. (25). The expression for R_a differs from that in Ref. [1], as we now include mode conversion and transmission. The Rayleigh criterion states that if R_a is smaller than $\pi/4$, the surface is relatively smooth, otherwise it is rough. Here we let R_a equal $\pi/4$ and calculate the critical σ values and find that they are almost the same as σ_{med} observed from Fig. 9 for all the modes. The underlying physics in this are that the peak appears at the intermediate σ_{med}, at which the surface starts to transit from smooth to rough according to the Rayleigh criterion.

In addition, we plot the specular transmission in Fig. 10 when only varying the wave speed $c_p^{(2)}$ of Solid 2. The trends as increasing σ are somewhat different from those when varying the density $\rho^{(2)}$ shown in Fig. 8. For instance, the value of σ_{med} increases when $c_p^{(2)}/c_p^{(1)}$ becomes larger, and it can still be accurately estimated by the Rayleigh criterion.

The role of the correlation length λ_0 on the specular scattering is also studied as shown in Fig. 11. The rms value is fixed as $\sigma = \lambda_p^{(1)}/10$ in this case. As can be seen there exists a linear dependence of the specular scattering on λ_0. In the specular direction the parameter A_β is zero and hence the exponential terms in Eq. (27) vanish, which clearly leads to the linear relationship between λ_0 and σ^d_{sc}. It should be noted that the simple linear dependence is found within the valid region of the Kirchhoff approximation [26]. For weakly correlated surfaces (λ_0 is very small) the linearity might break down, and it is argued to be caused by the energy converted from the surface waves [10].

V. IMPLICATIONS FOR BOUNDARY PHONON TRANSPORT

The phonons transmitted through the interface between two media are impeded by roughness and the reflections result in a thermal boundary resistance to heat flow. The thermal boundary conductance is defined as the ratio of the heat current

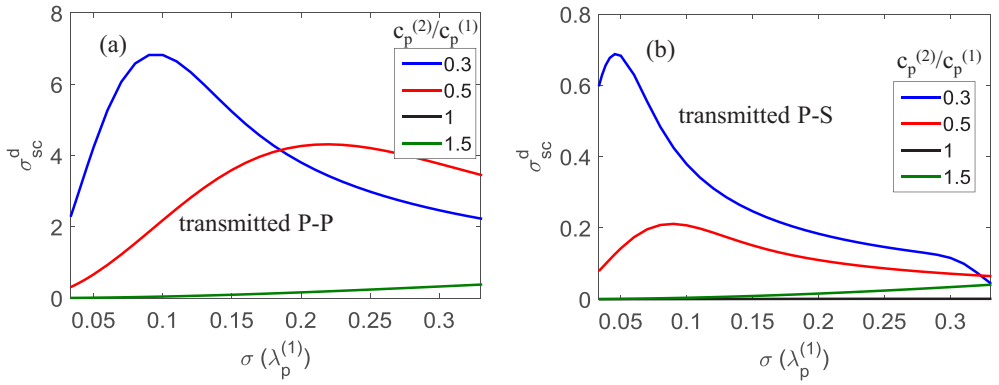

FIG. 10. Diffuse scattering cross section (σ_{sc}^d) at the specular direction from an interface (Solid 1 is Si; Solid 2 has the same density as Ge but various values of wave speed) by a 20° incident P wave as a function of rms values (σ) when the correlation length $\lambda_0 = 2\lambda_p^{(1)}$. (a) Transmitted P-P. (b) Transmitted P-S.

density and the temperature differential [35]:

$$G = \frac{1}{4\pi}\int_0^{2\pi} d\phi \int_0^{\pi/2} d\theta \int_0^{\omega_{D1}} v_1 \cos\theta \sin\theta \hbar\omega \frac{\partial f(\omega,T)}{\partial T} \times \tau_{12}(\omega,\phi,\theta) D(\omega) d\omega = \frac{1}{2}\int_0^1 \left[\int_0^{\omega_{D1}} v_1 \hbar\omega D(\omega)\frac{\partial f(\omega,T)}{\partial T}\tau_{12}(\omega,\cos\theta)d\omega\right] \times \cos\theta d\cos\theta, \quad (33)$$

where v_1 is the wave speed in Solid 1, $D(\omega)$ is the density of states for phonons, and $f(\omega,T)$ is the Bose-Einstein distribution for phonons at the temperature T. The second expression in Eq. (33) is obtained by assuming an isotropic medium. The accuracy of Eq. (33) depends on how the transmissivity is modeled, and this is significantly affected by the interface roughness.

Historically, the acoustic mismatch model (AMM) [35] has been widely used, which simply models the reflection and transmission according to the acoustic impedance contrast using the Fresnel coefficient from a flat surface, and hence it gives the transmissivity at the specular angle. We define the transmissivity from Solid 1 to Solid 2 as τ_{12}, and using AMM it is given by

$$\tau_{12} = \frac{4Z_1Z_2}{(Z_1+Z_2)^2}, \quad (34)$$

where Z_1 and Z_2 refer to the acoustic impedance in Solid 1 and 2, which are $v_1\rho_1/\cos\theta_i$ and $v_2\rho_2/\cos\theta_s$ respectively. Another crude method is called the diffuse mismatch model (DMM), which assumes that the phonons incident at the interface lose memory of their original state and hence one cannot tell from which side they have come [35,36]. In other words, the transmission probabilities are the same for all phonon states corresponding to the same frequency; this implies that the transmissivity from Solid 2 to Solid 1, τ_{21}, equals $1-\tau_{12}$. By further assuming a linear dispersion relationship, the transmissivity τ_{12} using DMM is obtained by Swartz and Pohl [37] as:

$$\tau_{12} = \frac{1/v_2^2}{1/v_1^2 + 1/v_2^2}. \quad (35)$$

The linear assumption implies that the phase velocity equals the group velocity, and it is approximately valid at low temperatures for wave vectors close to the zone center of the dispersion relationship [35]. Neither of these two models depends on the roughness nor the frequency, because AMM is obtained from limits of purely specular reflections from a flat interface, while DMM is approximated from limits of completely diffuse waves based on a perfectly rough interface; in addition, DMM is also independent of angles.

However, roughness plays a critical role in determining the transmissivity or the specularity parameters [38], and in Fig. 12(a) we show a comparison of the calculated specular transmissivity for the Si/Ge interface using four methods, namely, AMM, DMM, our method using the KA, and Ziman's formulas. The specular transmissivity is plotted with respect to a sub-THz range of frequencies (100 GHz to 600 GHz), when rms $\sigma = 4.2$ nm, and correlation length $\lambda_0 = 42$ nm. Note that the specular transmissivity using the KA is calculated as an integral of the scattering cross section within a narrow angular range around the specular angle. From Fig. 12(a), the curve calculated by the Kirchhoff approximation lies between the two dotted lines representing AMM and DMM. At low frequencies, the KA tends to the AMM result, and as the frequency increases KA tends to approach DMM when the

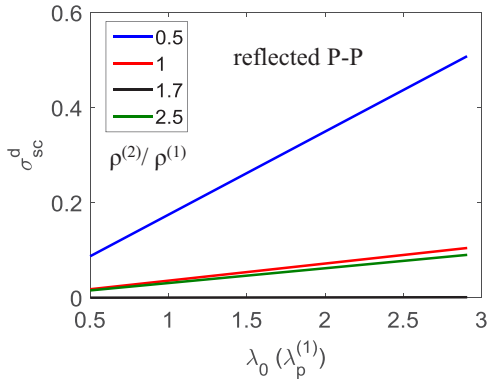

FIG. 11. Diffuse scattering cross section (σ_{sc}^d) for the reflected P-P mode at the specular direction from an interface (Solid 1 is Si; Solid 2 has the same wave speed as Ge but various values of the density) by a 20° incident P wave as a function of correlation length (λ_0) when the rms value $\sigma = \lambda_p^{(1)}/10$.

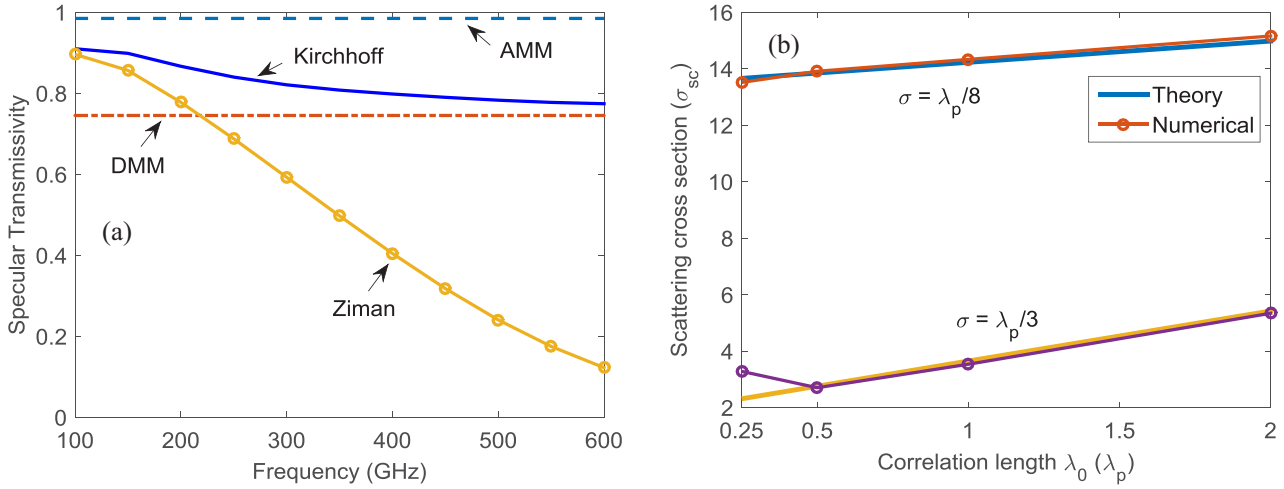

FIG. 12. (a) Comparison of the specular transmissivity using AMM, DMM, Ziman's formula, and the elastodynamic Kirchhoff theory as a function of frequency, when $\sigma = 4.2$nm, and $\lambda_0 = 42$ nm. (b) Comparison of the specular scattering cross section using the elastodynamic Kirchhoff theory and the numerical method when $\lambda_0 = \lambda_p/4$, $\lambda_p/2$, λ_p, and $2\lambda_p$.

diffuse field is significant. Hence, as seen in Fig. 12(a), the Kirchhoff method connects the results between the two limiting cases of AMM and DMM. The result using the Ziman's formula Eq. (1) is also plotted for comparison, which is accurate only in the range of low frequencies, but dramatically underestimates the transmissivity at higher frequencies as it ignores the diffuse field. Although it still relies upon linear dispersion, the KA can be considered superior to AMM, DMM, and Ziman's formulas, which only give rough estimates of the phonon scattering. Therefore, the method developed could improve the agreement of Eq. (33) with experimental results, by modeling the transmissivity more accurately. It is also worth noting that the elastodynamic Kirchhoff method developed here does have limitations as it is based on the assumption of a linear, homogeneous, and isotropic bulk medium, unlike more sophisticated numerical full atomistic simulation methods that include crystallographic orientations and surface structures.

The region of validity for KA has been evaluated [26] for surfaces with stress-free boundary conditions, hence only including reflections. Here we show the validity of the KA for modeling transmission through a rough interface by comparing the theoretical results and the mean results from Monte Carlo simulations as deployed in Sec. III. The difference here is that we now reduce the correlation length λ_0 from $2\lambda_p$ to $\lambda_p/4$. Figure 12(b) shows the specular scattering cross section for different correlation lengths with both low and high rms values. As can be seen, the Kirchoff method is very accurate when λ_0 is larger or equal than $\lambda_p/2$, below which the KA breaks down. The criteria here show when the use of KA for rough interface transmission is valid, which also has implications for the use of Eq. (33) to model the thermal boundary conductance with KA.

VI. CONCLUSIONS

In this article, we have derived theoretical formulas to predict the diffuse field of elastic waves scattered and transmitted by rough solid-solid interfaces, by using the Kirchhoff approximation. Theoretical solutions are evaluated by comparison with numerical Monte Carlo simulations, and the theory is shown to be accurate for surfaces with rms value σ up to $\lambda/3$. The new capability to model the diffuse field over a much wider range of roughness, beyond the limit of the small perturbation theory, enables the investigation of how interface roughness affects scattering when the rms value is large. Generally speaking, the reflection and transmission are found to have different dependence on the interface roughness, and also a strong dependence on the material properties. As expected, the impedance mismatch plays an important role in determining the diffuse scattering, while it is found that the effects from the mismatch of density and wave speed are different. For the Si/Ge interface evaluated here, the transmission of waves from Si to Ge is much less affected by the interface roughness than the reflection. As a result, the reflection diffuse energy tends to be more widely spread, and a shift of the peak of the reflection pattern away from the specular direction can be observed for interfaces with high roughness. In the extreme case when the two solids have the same wave speed, the transmission is only coherent and it is the same as that traveling through a flat interface. In addition, there exists an intermediate value of rms at which the diffuse energy in the specular direction reaches its maximum, and this rms value coincides with that estimated by the Rayleigh criterion, indicating that the conventional Rayleigh criterion is a precise measure of the transition point when the interface becomes rough. It is also found that at the specular direction the scattering energy linearly depends on the correlation length within the valid region of the Kirchhoff approximation.

Most current studies in phonon transport are based either on Ziman's formulas only modeling the coherent field, or the diffuse mismatch model, assuming a perfect rough surface that scatters waves to any direction with an equal probability, for the diffuse field. Implications for the phonon transport through rough interfaces are discussed in Sec. V, and a comparison among different methods in terms of the transmissivity is shown. The method developed in this paper provides a strong analytical tool that connects these hypotheses in limiting cases.

The new theory could be potentially useful for calculating the thermal boundary conductance, and may assist interpreting experimental phenomena of thermal transport in nanostructures [9,13], which are not well understood.

ACKNOWLEDGMENTS

We thank Dr. Vincenzo Giannini and Dr. Menglong Hao for discussion and encouragement. This research was supported by the UK research center in NDE.

[1] J. A. Ogilvy, *Theory of Wave Scattering from Random Rough Surfaces* (Adam Hilger, Bristol, 1991).
[2] J. A. Ogilvy and J. R. Foster, J. Phys. D: Appl. Phys. **22**, 1243 (1989).
[3] J. A. Ogilvy and I. D. Culverwell, Ultrasonics **29**, 490 (1991).
[4] J. Pettit, A. E. Walker, and M. J. S. Lowe, IEEE Trans. Ultrason. Ferroelectr. Freq. Control. **62**, 1797 (2015).
[5] F. Shi, M. J. S. Lowe, X. Xi, and R. V. Craster, J. Mech. Phys. Solids **92**, 260 (2016).
[6] J. Sadhu and S. Sinha, Phys. Rev. B **84**, 115450 (2011).
[7] J. Carrete, L. J. Gallego, L. M. Varela, and N. Mingo, Phys. Rev. B **84**, 075403 (2011).
[8] H. Sun and K. P. Pipe, J. Appl. Phys. **111**, 023510 (2012).
[9] J. B. Hertzberg, M. Aksit, O. O. Otelaja, D. A. Stewart, and R. D. Robinson, Nano Lett. **14**, 403 (2014).
[10] A. A. Maznev, Phys. Rev. B **91**, 134306 (2015).
[11] A. A. Maznev, F. Hofmann, J. Cuffe, J. K. Eliason, and K. A. Nelson, Ultrasonics **56**, 116 (2015).
[12] Y.-C. Wen, C.-L. Hsieh, K.-H. Lin, H.-P. Chen, S.-C. Chin, C.-L. Hsiao, Y.-T. Lin, C.-S. Chang, Y.-C. Chang, L.-W. Tu, and C.-K. Sun, Phys. Rev. Lett. **103**, 264301 (2009).
[13] J. Cuffe, O. Ristow, E. Chávez, A. Shchepetov, P.-O. Chapuis, F. Alzina, M. Hettich, M. Prunnila, J. Ahopelto, T. Dekorsy, and C. M. Sotomayor Torres, Phys. Rev. Lett. **110**, 095503 (2013).
[14] J. A. Ogilvy, NDT Int. **19**, 371 (1986).
[15] R. Chen, A. I. Hochbaum, P. Murphy, J. Moore, P. Yang, and A. Majumdar, Phys. Rev. Lett. **101**, 105501 (2008).
[16] J. S. Heron, T. Fournier, N. Mingo, and O. Bourgeois, Nano Lett. **9**, 1861 (2009).
[17] Z. Aksamija and I. Knezevic, Phys. Rev. B **82**, 045319 (2010).
[18] J. M. Ziman, *Electrons and Phonons* (Clarendon Press, Oxford, 1960).
[19] J. Weber, W. Sandmann, W. Dietsche, and H. Kinder, Phys. Rev. Lett. **40**, 1469 (1978).
[20] Z. Wang, J. E. Alaniz, W. Jang, J. E. Garay, and C. Dames, Nano Lett. **11**, 2206 (2011).
[21] F. Shi, W. Choi, E. A. Skelton, M. J. S. Lowe, and R. V. Craster, IEEE Trans. Ultrason. Ferroelectr. Freq. Control **61**, 2054 (2014).
[22] H. Zhao and J. B. Freund, J. Appl. Phys. **105**, 013515 (2009).
[23] Z. Liang, K. Sasikumar, and P. Keblinski, Phys. Rev. Lett. **113**, 065901 (2014).
[24] E. I. Thorsos and D. R. Jackson, J. Acoust. Soc. Am. **86**, 261 (1989).
[25] E. I. Thorsos, J. Acoust. Soc. Am. **83**, 78 (1988).
[26] F. Shi, W. Choi, E. A. Skelton, M. J. S. Lowe, and R. V. Craster, Proc. R. Soc. A **471**, 1 (2015).
[27] L. D. Landau and E. M. Lifshitz, *Theory of Elasticity*, 2nd ed. (Pergamon Press, Oxford, 1970).
[28] K. F. Graff, *Wave Motion in Elastic Solids* (Oxford University Press, Oxford, 1975).
[29] J. D. Achenbach, *Reciprocity in Elastodynamics* (Cambridge University Express, Cambridge, 2003).
[30] M. V. Berry, Contemp. Phys. **56**(1), 2 (2015).
[31] C. A. Schultz and M. N. Tokosz, Geophys. J. Int. **117**, 783 (1994).
[32] P. Huthwaite, J. Comput. Phys. **257**, 687 (2014).
[33] P. Rajagopal, M. Drozdz, E. A. Skelton, M. J. S. Lowe, and R. V. Craster, NDT and E Int. **51**, 30 (2012).
[34] P. Nagy and J. H. Rose, J. Appl. Phys. **73**, 566 (1993).
[35] G. Chen, *Nanoscale Energy Transport and Conversion: A Parallel Treatment of Electrons, Molecules, Phonons, and Photons* (Oxford University Express, New York, 2005).
[36] P. Reddy, K. Castelino, and C. Majumdar, Appl. Phys. Lett. **87**, 211908 (2005).
[37] E. T. Swartz and R. O. Pohl, Rev. Mod. Phys. **61**, 605 (1989).
[38] D. Li and A. J. H. McGaughey, Nanosc. Microsc. Therm. **19**, 166 (2015).